RESEARCH ARTICLE | MARCH 08 2018

Numerical investigation on the dynamics and evolution mechanisms of multiple-current-pulse behavior in homogeneous helium dielectric-barrier discharges at atmospheric pressure

Yuhui Zhang; Wenjun Ning ; Dong Dai

AIP Advances 8, 035008 (2018)
https://doi.org/10.1063/1.5019815

AIP ADVANCES **8**, 035008 (2018)

Numerical investigation on the dynamics and evolution mechanisms of multiple-current-pulse behavior in homogeneous helium dielectric-barrier discharges at atmospheric pressure

Yuhui Zhang, Wenjun Ning, and Dong Dai[a]
School of Electric Power, South China University of Technology, Guangzhou 510641, China

(Received 17 December 2017; accepted 26 February 2018; published online 8 March 2018)

A systematic investigation on the dynamics and evolution mechanisms of multiple-current-pulse (MCP) behavior in homogeneous dielectric barrier discharge (HDBD) is carried out via fluid modelling. Inspecting the simulation results, two typical discharge regimes, namely the MCP-Townsend regime and MCP-glow regime, are found prevailing in MCP discharges, each with distinctive electrical and dynamic properties. Moreover, the evolution of MCP behavior with external parameters altering are illustrated and explicitly discussed. It is revealed that the discharge undergoes some different stages as external parameters vary, and the discharge in each stage follows a series of distinctive pattern in morphological characteristics and evolution trends. Among those stages, the pulse number per half cycle is perceived to observe non-monotonic variations with applied voltage amplitude (V_{am}) and gap width (d_g) increasing, and a merging effect among pulses, mainly induced by the enhanced contribution of sinusoidal component to the total current, is considered responsible for such phenomenon. The variation of incipient discharge peak phase (Φ_{pm}) is dominated by the value of V_{am} as well as the proportion of total applied voltage that drops across the gas gap. Moreover, an abnormal, dramatic elevation in J_{pm} with d_g increasing is observed, which could be evinced by the strengthened glow discharge structure and therefore enhanced space charge effect. *© 2018 Author(s). All article content, except where otherwise noted, is licensed under a Creative Commons Attribution (CC BY) license (http://creativecommons.org/licenses/by/4.0/).* https://doi.org/10.1063/1.5019815

I. INTRODUCTION

Recently there have been tremendously growing interests in homogeneous dielectric-barrier discharge (HDBD) operated at atmospheric pressure due to its immense potentials for numerous industrial applications, such as surface modification,[1,2] biomedical sterilization[3–5] and pollution control.[6] Typically, the temporal waveform of atmospheric HDBD is characterised by one narrow current pulse per half cycle of applied voltage under traditional parallel-plate discharge structure.[7–9] However, in many cases, HDBDs with 2 or more current pulses per half cycle is also perceived. This phenomenon, entitled 'multiple current pulses (MCP) discharge',[10] or 'pulsed regime diffuse discharge',[11] 'pseudo-glow discharges',[12] was convinced and studied in massive previous reports.[7,10–18]

The early investigations on the MCP behavior in homogeneous gas discharge system could date back to 1960s when Bartnikas *et al.*[18,19] studied the discharge rate and energy loss of metallic electrode discharges at atmospheric pressure. Voltage waveforms with multiple peaks per half cycles were obtained and the oscillation rates were found differ under different applied voltage. Entering the 2000s, Akishev *et al.*[11] established a simplified one-dimensional numerical model to study the origin

---

[a] Author to whom correspondence should be addressed. Electronic mail: ddai@scut.edu.cn

of MCP discharge and proposed that the MCP is formed because of a negative differential resistance of the cathode fall region, which essentially occupies the entire discharge gap in each half cycle of the applied voltage. Zhang *et al.*[20] also emphasized the significance of negative differential resistance on the formation of MCP, and the corresponding phase-space trajectory plots were presented to support their standpoint. Golubovskii *et al.*[7] regarded the MCP as the oscillations of the discharge system in the vicinity of the equilibrium position and obtained its relevant intrinsic frequency and damping factor through theoretical methods. Shin *et al.*[9] investigated the evolution of MCP behaviors with driving frequency altering via experiments and a simple dynamic model, finding that an increase in frequency caused the decrease in the number of pulses and pulse widths in each discharge half cycle. They also developed a preliminary approach to control the MCP behavior via a "ramp-plus-plateau" voltage input. Petrovic *et al.*[21] performed the similar parametric study in a coaxial structure HDBD and observed identical evolution trends of MCP as those conducted in parallel-plate structure HDBDs.

While the fundamental insights into the MCP discharges have been obtained, a substantial amount of other aspects, however, still remain the subject of debate. For example, a unique "merging" effect among pulses along with the non-monotonic evolution of pulse number were observed in some previous studies,[15,21] which is quite different from the common knowledge, while the detailed mechanism of this phenomenon has not been made clear. Moreover, the mode transitions during the discharge epoch of MCP was investigated by Jiang *et al.*,[13] a complicated evolution from the Townsend mode, through glow, Townsend, and glow, and finally back to the Townsend one is observed, while the initiation as well as transition criteria of those modes have not been fully understood. From this perspective, the HDBD-driven MCP discharge still requires more in-depth investigations.

In this paper, a one-dimensional fluid model is applied to investigate the influence of external parameters on MCP behavior in HDBDs. Some new features regarding the dynamics and evolutions of MCP discharges are observed and analysed. The paper is organized as follows: Section II describes the numerical model applied in this work. Results obtained in the numerical simulation and its relevant discussions are shown in Section III. Some conclusive remarks are put forward in Section IV.

II. MODEL DESCRIPTION

The atmospheric DBD considered here is generated in pure helium gap between two dielectrically insulated parallel-plate electrodes. The thickness of each dielectric layer d_b is 1 mm and the relative permittivity ε_r is set to be 7.5, corresponding to the value of mica glass. The width of discharge gap is flexible, with atmospheric helium gas filling in at the temperature of 300 K. Electrodes are considered as disk-shaped, with the area of 0.01 m^2 each. A sinusoidal voltage with the amplitude V_{am} and the frequency f is applied on the upper electrode, the other electrode is grounded. Note that the discharge gap considered in this paper is not very large (under 5 mm), much shorter than the radius of electrodes (about 56.4 mm), therefore, the discharge considered here can be assumed homogeneous radially. Under the conditions mentioned above, a one-dimensional fluid model is appropriate to simulate the discharge process, which has also been successfully applied to investigate the MCP phenomena in previous reports.[7,9,13,22,23] The schematic of the model is illustrated in Figure 1.

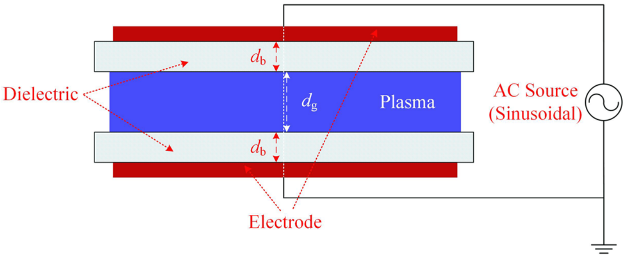

FIG. 1. Schematic of the model. d_g and d_b represent the gas gap width and width of dielectric layer, respectively.

In this model, electron number density and energy density are determined by the Boltzmann equation, and simplified to the continuity equations through drift-diffusion approximation:[24–28]

$$\frac{\partial n_{\mathrm{e}}}{\partial t} + \nabla \cdot \boldsymbol{\Gamma}_{\mathrm{e}} = S_{\mathrm{e}} \tag{1}$$

$$\frac{\partial n_{\varepsilon}}{\partial t} + \nabla \cdot \boldsymbol{\Gamma}_{\varepsilon} = S_{\varepsilon} - \boldsymbol{E} \cdot \boldsymbol{\Gamma}_{\varepsilon} \tag{2}$$

$$\boldsymbol{\Gamma}_{\mathrm{e}} = -\mu_{\mathrm{e}} n_{\mathrm{e}} \boldsymbol{E} - D_{\mathrm{e}} \nabla \cdot n_{\mathrm{e}} \tag{3}$$

$$\boldsymbol{\Gamma}_{\varepsilon} = -\frac{5}{3} \mu_{\mathrm{e}} n_{\varepsilon} \boldsymbol{E} - \frac{5}{3} D_{\mathrm{e}} \nabla \cdot n_{\varepsilon} \tag{4}$$

where n_{e}, n_{ε} represent the electron number density and energy density, respectively. $\boldsymbol{\Gamma}_{\mathbf{e}}$, and $\boldsymbol{\Gamma}_{\boldsymbol{\varepsilon}}$ are the total electron flux and electron energy flux. S_{e} is the source term describing the net changing rate of electron density due to chemical reactions, S_{ε} is the electron energy source term accounting for the loss or gain of energy from collisions between electrons and heavy species. μ_{e}, D_{e} represent electron mobility and diffusion coefficient, respectively, whose values are calculated by Bolsig+[29] and tabulated as the functions of mean electron energy, while these of the heavy particles are taken from literatures.[30,31] Detailed input parameters for Bolsig+ solver are listed in Table I. $\boldsymbol{E}$ is the local electric field. The term $\boldsymbol{E}\cdot\boldsymbol{\Gamma}_{\boldsymbol{\varepsilon}}$ accounts for the contribution of Joule heat. With n_{ϵ} determined, the electron temperature T_{e} (in K) can be obtained through:[28]

$$\overline{\varepsilon} = \frac{n_{\varepsilon}}{n_{\mathrm{e}}} = \frac{3}{2} k_{\mathrm{B}} T_{\mathrm{e}} \tag{5}$$

where k_{B} represents the Boltzmann constant, $\overline{\varepsilon}$ stands for electron mean energy.

For heavy species in the mixture, their transport properties are described by multi-component equation:[26,27]

$$\rho_{\mathrm{m}} \frac{\partial (w_k)}{\partial t} = \nabla \cdot \boldsymbol{\Gamma}_k + S_k \tag{6}$$

where w_k represents the mass fraction of heavy species k, ρ_{m} is the density of the mixture, S_k is the source term, $\boldsymbol{\Gamma}_{\mathbf{k}}$ represents drift-diffusion flux for species k.

Electric field is determined from Poisson's Equation, describing as

$$\nabla \cdot (\varepsilon_0 \varepsilon_{\mathrm{r}} \boldsymbol{E}) = -\nabla \cdot (\varepsilon_0 \varepsilon_{\mathrm{r}} \nabla V) = \rho_{\mathrm{sp}} \tag{7}$$

in which ε_0, ε_{r} stand for the permittivity of vacuum and relative permittivity, respectively. V is the potential and ρ_{sp} is the space charge density in the discharge gap.

On the boundaries of the gas gap (i.e. interface with dielectric surfaces), excited species are quenched to helium atoms, and secondary electrons are induced by ion bombardment with a emission coefficient γ_{i} of 0.01, their initial mean energy are fixed at 2.5 eV. Detailed surface reactions are listed in Table II.

The resulting equations for the normal component of electron flux on the boundaries are given by[24,26,27,33]

$$\mathbf{n} \cdot \boldsymbol{\Gamma}_{\mathbf{e}} = \frac{1}{2} \sqrt{\frac{8 k_{\mathrm{B}} T_{\mathrm{e}}}{\pi m_{\mathrm{e}}}} n_{\mathrm{e}} - \alpha_{\mathrm{s}} n_{\mathrm{e}} \mu_{\mathrm{e}} \boldsymbol{E} \cdot \mathbf{n} - \sum \gamma_{\mathrm{i}} N_{\mathrm{A}} (\mathbf{n} \cdot \boldsymbol{\Gamma}_{\mathbf{i}}) \tag{8}$$

$$\mathbf{n} \cdot \boldsymbol{\Gamma}_{\varepsilon} = \frac{5}{6} \sqrt{\frac{8 k_{\mathrm{B}} T_{\mathrm{e}}}{\pi m_{\mathrm{e}}}} n_{\varepsilon} - \alpha_{\mathrm{s}} n_{\varepsilon} \mu_{\mathrm{e}} \boldsymbol{E} \cdot \mathbf{n} - \sum \gamma_i \overline{\varepsilon_0} N_{\mathrm{A}} (\mathbf{n} \cdot \boldsymbol{\Gamma}_{\mathbf{i}}) \tag{9}$$

TABLE I. Input parameters for Bolsig+ solver. Note: T_{g} represents the gas temperature.

EEDF type	Database used	Energy range	T_{g}	Ionization degree	Electron density
Boltzmann	IST-Lisbon[32]	0.1~50 eV	300 K	10^{-7}	10^{19} m^{-3}

TABLE II. Surface reactions considered in the model.

Num.	Formula	Reaction probability	γ_i	Initial electron mean energy
1	He^+ => He	1	0.01	2.5
2	$He_2{}^+$ => 2He	1	0.01	2.5
3	He^* => He	1	0	0
4	$He_2{}^*$ => 2He	1	0	0

where m_e represents electron mass, $\boldsymbol{\Gamma}_\mathbf{i}$ stands for ion flux on the interface, **n** is the unit normal vector pointing towards the solid surface, N_A represents the Avogadro constant. α_s is a switching function depending on the product of $\boldsymbol{E}\cdot\mathbf{n}$, defined as

$$\alpha_s = \begin{cases} 1\ (\mathrm{sgn}(q)\boldsymbol{E}\cdot\mathbf{n} \geq 0) \\ 0\ (\mathrm{sgn}(q)\boldsymbol{E}\cdot\mathbf{n} < 0) \end{cases} \tag{10}$$

where sgn(q) represents the sign of the charge q for considered species. For heavy species flux, their boundary conditions on the solid surfaces are described by:[26]

$$\mathbf{n}\cdot\boldsymbol{\Gamma}_k = M_k R_{s,k} + \alpha_s M_k c_k \mu_{k,m} z_k \boldsymbol{E}\cdot\mathbf{n} \tag{11}$$

where $\boldsymbol{\Gamma_k}$ stands for flux term for species k. M_k, c_k, z_k represent the molar weight, the mass fraction and the charge number of species k, respectively. $\mu_{k,m}$ is the mixture-averaged mobility. $R_{s,k}$ is the relevant surface reaction rate given by[26,34]

$$R_{s,k} = c_k \sum_{i=1}^{N} v_{i,k} \frac{\gamma_m}{1-\gamma_m/2} \frac{1}{4} \sqrt{\frac{8\mathrm{R}T_g}{\pi m_m}} \tag{12}$$

in which N represents the number of surface reactions, R is the universal gas constant, $v_{i,k}$ is the stoichiometric number of species k on the ith surface reaction, γ_m is known as sticking coefficient showing the occurring probability of the reaction, and the term $\gamma_m/(1\text{-}\gamma_m/2)$ represents Motz–Wise correction.[34] m_m is the mean mass of the mixture. T_g is the gas temperature, having the assumption $T_g = T_i = T_m = 300$ K. (T_i, T_m are ion temperature and mixture temperature, respectively).

The boundary conditions for surface charge accumulation are given by

$$\frac{d\sigma_s}{dt} = \boldsymbol{J}_e\cdot\mathbf{n} + \boldsymbol{J}_i\cdot\mathbf{n} \tag{13}$$

$$\sigma_s = (\boldsymbol{D}_2 - \boldsymbol{D}_1)\cdot\mathbf{n} \tag{14}$$

where σ_s represents surface charge density, J_e and J_i are the total electron and ion current densities on the wall. D_1 and D_2 are the electric displacement vectors on both side of the boundary.

About plasma chemistry, 6 particles, namely the electron (e), He atom, He metastable (He^*), He_2 metastable ($He_2{}^*$), He^+ and $He_2{}^+$, and 27 reactions are considered. Detailed reaction formulas are listed in Table III, in which some of the rate coefficient data are taken from literatures.[29,32,35–41] Air impurities and their relevant reactions are not included in this model. Considering their capability of reshaping the current waveform,[7,26,27,42,43] chances are that these air traces would function on MCP phenomena. However, in view of the successful use of pure-helium models to reproduce relevant experimental results in many previous MCP reports[9,15,23] as well as the issue of time efficiency during the calculation, we choose to exclude air impurities in the model for the sake of simplicity, and try out best to match the simulation results with that of experimental ones by adjusting the configuration and external parameters of the discharge system. Besides, the initial densities of electron and ions (He^+ and He^+) are set to be 1×10^{13} m^{-3}, 5×10^{12} m^{-3} and 5×10^{12} m^{-3} respectively to maintain the initial charge balance. Those initial conditions are common assumptions used in DBD modelling. Within logical parameter ranges, these input values did not show any obvious effect on the solution, just causing minor differences in calculation time.

The equations mentioned above are discretized through finite element method and solved in COMSOL MULTIPHYSICS 5.2.[44] A direct solver PARDISO[45,46] is employed in the program to

TABLE III. Chemical reactions considered in the model. Note: T_e denotes the electron temperature in eV. He* represents He(2^3S) and He(2^1S). He_2^* represents $He_2(a^3\Sigma_u^+)$. n_e is the electron density in m^{-3}. The unit of reaction rate coefficient for two body reactions and three body reactions are m^3/s and m^6/s, respectively. $f(T_e)$ indicates the rate coefficient as a function of the electron mean energy calculated by Bolsig+,[32] whose input parameters are shown in Table I.

Num.	Formula	Rate coefficient	Energy/eV	Ref.
1	$e+He => e+He$	$f(T_e)$	/	29,32
2	$e+He => e+He^*$	$f(T_e)$	19.82	29,32
3	$e+He => e+He^+$	$f(T_e)$	24.59	29,32
4	$e+He^* => 2e+He^+$	$1.28\times10^{-7}\times T_e^{0.6}\times\exp(-4.78/T_e)$	4.78	35
5	$e+He^* => e+He$	2.9×10^{-9}	-19.82	26,35
6	$e+He_2^* => e+2He$	3.8×10^{-9}	-17.9	26,35
7	$2e+He^+=>e+He^*$	$5.82\times10^{-20}\times(T_e/0.026)^{-4.4}$	-4.78	26,32
8	$2e+He_2^+ => He^*+He+e$	2.8×10^{-20}	0	26,32
9	$e+He+He_2^+ => He^*+2He$	3.5×10^{-27}	0	26,32
10	$2e+He_2^+ =>He_2^*+e$	1.2×10^{-21}	0	26,32
11	$e+He+He_2^+ => He_2^*+He$	1.5×10^{-27}	0	26,32
12	$e+He^+ => He^*$	$6.76\times10^{-13}\times T_e^{-0.5}$	0	36
13	$e+He+He^+=> He+He^*$	$1\times10^{-26}\times(T_e/0.026)^{-2}$	0	37
14	$e+He_2^+ => He^*+He$	$8.82\times10^{-9}\times(T_e/0.026)^{-1.5}$	0	37
15	$e+He_2^+ =>2He$	1.0×10^{-8}	0	37
16	$e+He+He_2^+=> 3He$	2.0×10^{-27}	0	26,32
17	$e+He_2^* => 2e+He_2^+$	$9.75\times10^{-16}\times T_e^{0.71}\times\exp(-3.4/T_e)$	3.4	36
18	$He^*+2He=>3He$	2.0×10^{-34}	/	26,32
19	$He^*+He^* => e+He_2^*$	2.03×10^{-9}	/	26,32
20	$He^*+He^* => e+He+He^+$	8.7×10^{-10}	/	7,38
21	$He^++2He => He_2^++He$	1.4×10^{-31}	/	39
22	$He^*+2He => He_2^*+He$	2.0×10^{-34}	/	40
23	$He^*+He_2^* => He^++2He+e$	5.0×10^{-10}	/	7
24	$He^*+He_2^* => He_2^++He+e$	2.0×10^{-9}	/	41
25	$He_2^*+He_2^* => He^++3He+e$	3.0×10^{-10}	/	41
26	$He_2^*+He_2^* => He_2^++2He+e$	1.2×10^{-9}	/	7
27	$He_2^*+He => 3He$	1.5×10^{-15}	/	37

solve the resulting system. About meshing strategy, two extremely fine meshed layers are set in the vicinity of each boundary in order to prevent the oscillation of particle density values in the simulation, each with the length of 0.02 mm and the average mesh density of $3000000\cdot m^{-1}$ (the average mesh density here is determined by the ratio between total mesh number in a certain meshing domain and the geometrical length of this domain). The size of mesh in these two layers follows an arithmetic sequence distribution with an element ratio of 10. The closer the mesh is to the boundary, the smaller its size will be. In the rest of the gap the mesh density is set smaller, with the average mesh density of $150000\cdot m^{-1}$ and the element ratio of 10. The number of elements in each calculation ranges from 232 to 762, varying with the gap width, and the number of degrees of freedom varies within 1050~5090. It is worth noting that the simulation results have been compared with those yielded from finer mesh calculations, and a maximum difference of ~1% in current density amplitude was perceived.

The simulation program is executed in a Dell T1700 station (CPU: E3-1226 3.30 GHz, RAM size: 20 G). Over 30 discharge cycles are calculated in each case to ensure that the discharge have evolved into steady state, and the time consumption for a single calculation ranges from 6 min to about 335 min, depending on the value of external parameters. Generally, a higher d_g and a lower f lead to the extension of calculation time.

III. RESULTS AND DISCUSSIONS

A. Electrical characteristics of MCP discharges

Under the simulation condition described above, the influence of external parameters including the applied voltage amplitude (V_{am}), driving frequency (f), and interelectrode gap width (d_g) on the electrical characteristics of MCP behavior in relatively short gap (within 4 mm) HDBDs are investigated. By altering the voltage amplitude with other external conditions remain unvaried, the influence of voltage amplitude on the MCP behavior is firstly studied. Figure 2 illustrates the temporal profiles of applied voltage (V_a), gap voltage (V_g), as well as total discharge current density (J_{tot}) with V_{am} altering, in which f and d_g are fixed at 10 kHz and 1 mm, respectively. As it can be seen, when V_{am} remains low, discharge with single current pulse per half cycle is observed, as shown in Figure 2(a). Gradually increasing V_{am} ranging from 0.8 kV to about 1.2 kV leads to a rise in pulse number per half cycle (N_p), in the meantime the phase of discharge epoch encounters an observably forward shifting, as shown in Figure 2(b), (c). If V_{am} is increased further, the enhancement in the number of pulses ceases, while the time intervals between the discharge peaks are narrowed, and the pulses tend to overlap each other, as shown in Figure 2(d) and 2(e). Continuously elevating V_{am} after exceeding about 2.8 kV, the waveform of current density is prone to stabilize, exhibiting a sinusoidal characteristic with a wide single pulse per half cycle, as shown in Figure 2(f), while the peak phase of the current pulse also tends to stabilize in the vicinity of 0° in this process. The above-mentioned phenomena are in principle consistent with experimental and numerical results obtained by previous studies.[7,10,12,15,21]

A decrease in driving frequency is also found in favour of the generation of MCP. Figure 3 illustrates the temporal profiles of applied voltage (V_a), gap voltage (V_g) as well as total current density (J_{tot}) with f altering, where V_a and d_g are fixed at 1.5 kV and 1 mm, respectively. As is shown

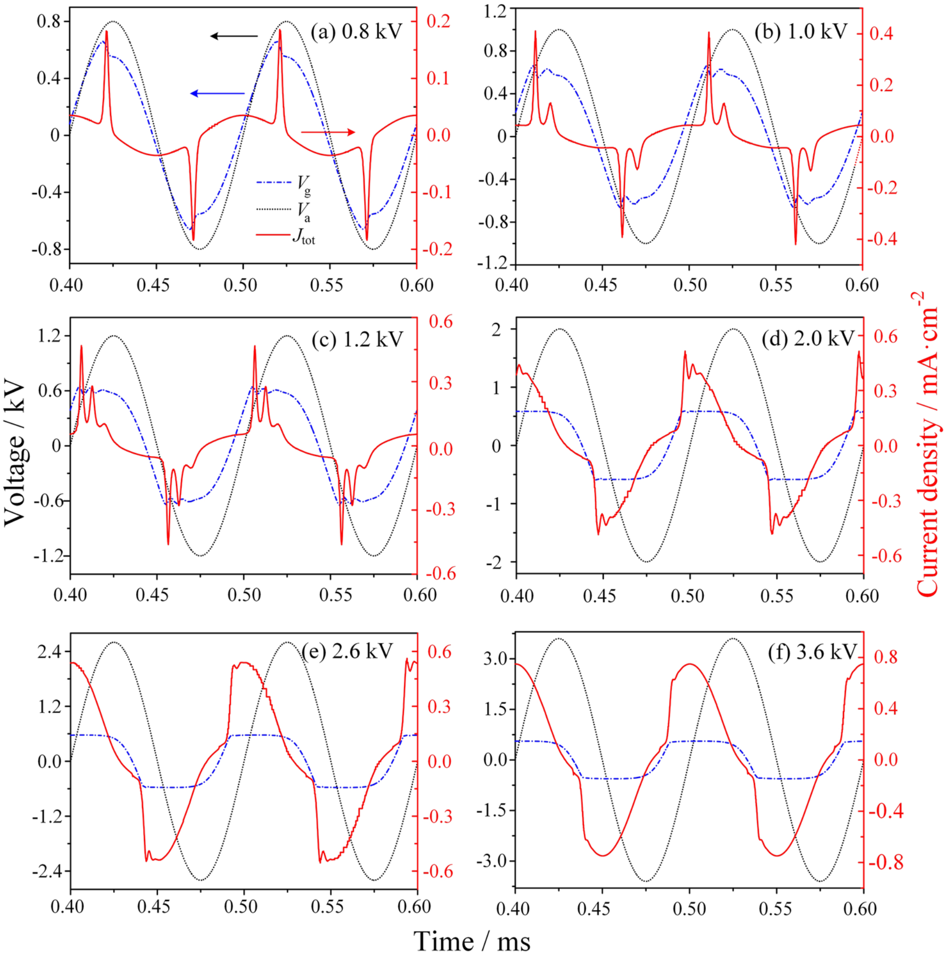

FIG. 2. Waveforms of applied voltage (V_a), gap voltage (V_g) as well as total current density (J_{tot}) at different voltage amplitudes (a)-(f). The driving frequency and gap width are fixed at 10 kHz and 1 mm, respectively.

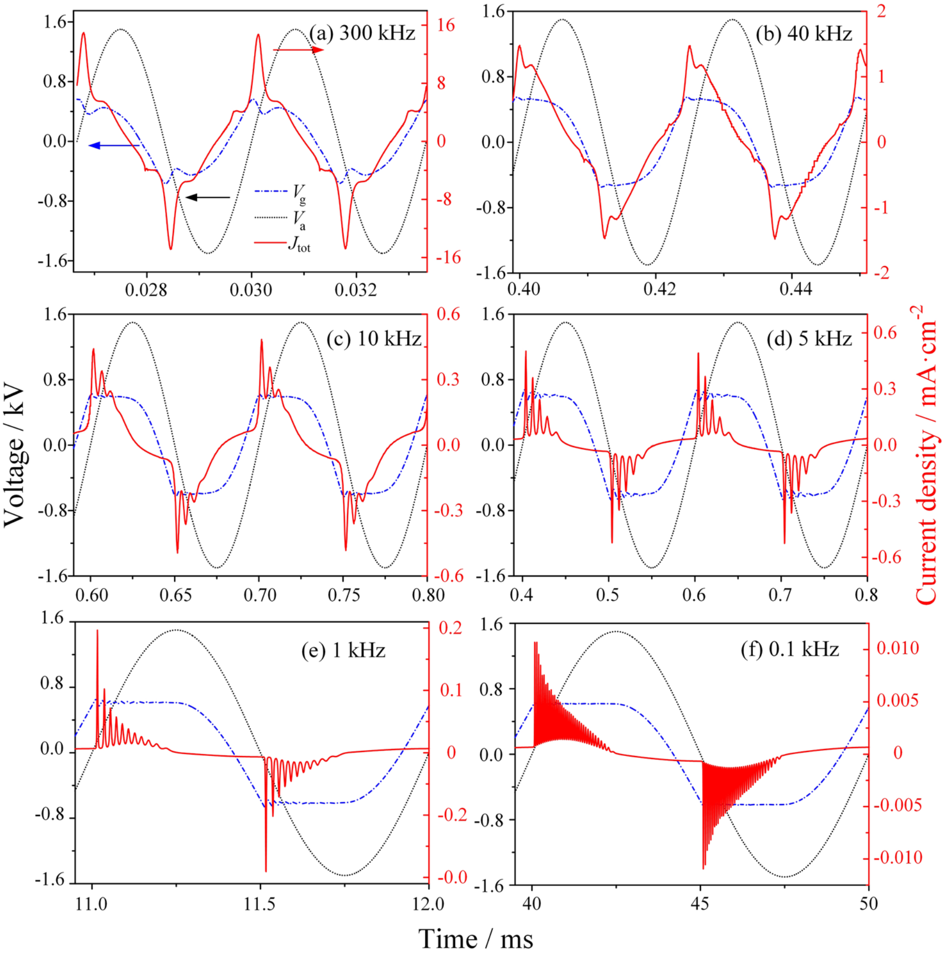

FIG. 3. Waveforms of applied voltage (V_a), gap voltage (V_g) as well as total current density (J_{tot}) under different driving frequencies (a)-(f). The voltage amplitude and gap width are fixed at 1.5 kV and 1 mm, respectively.

in Figure 3, in all cases, the number of pulses increases with frequency decreasing, and exhibiting a dramatic increase below 1 kHz, while the peak phase of first current pulse varies slightly. To be specific, in relatively high frequency range, single pulse discharge with a wide pulse is observed, as shown in Figure 3(a). Decreasing f promotes a subsequent discharge to be generated, initiating the MCP, as shown in Figure 3(b). Further decrease f leads to a continuous increase in pulse numbers per half cycle, as depicted in Figure 3(c), (d). A burst increase in N_p is observed when f is down to 1 kHz, as illustrated in Figure 3(e), (f). Such evolution trend is in good agreement with previous experimental and numerical results.[9,12,21]

The MCP evolution with interelectrode gap width d_g altering is illustrated in Figure 4. Analogous to previous results, in relatively large gaps, the discharge is prone to retain a single peak feature, as shown in Figure 4(a). A decrease in d_g leads to the increase of pulse number N, as shown in Figure 4(b), (c), while the pulses start to overlap each other when d_g decreases to certain ranges, as shown in Figure 4(d), (e), (f), which is similar to the evolution trace when V_{am} is chosen as the controlling parameter. Meanwhile, the first discharge pulses come in advance due to the decreasing breakdown voltage over the gap. Such evolution trace agrees well with the results obtained by Wang *et al.*[15] However, if continuous reducing the gap width to below 0.5 mm, the overlap of pulses ceases and N_p grows again, while the phase of first discharge pulse Φ_{pm} starts to move backwards, as shown in Figure 4(g), (h), (i). The non-monotonous evolution of N_p and Φ_{pm} reflect the complexity and diversity of MCP discharges.

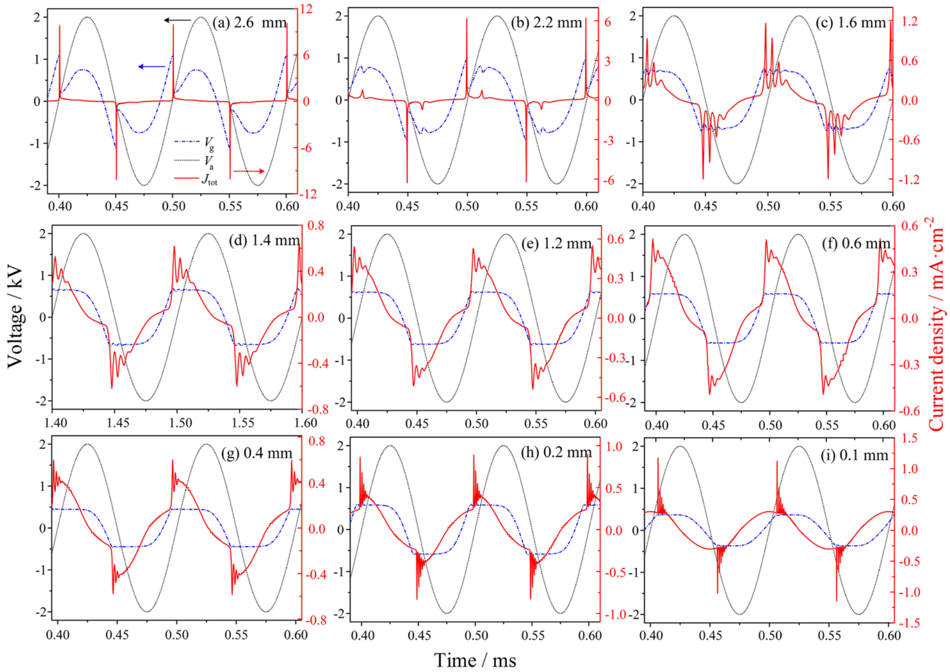

FIG. 4. Waveforms of applied voltage (V_a), gap voltage (V_g) as well as total current density (J_{tot}) under different gap width (a)-(i). The voltage amplitude and driving frequency are fixed at 2.0 kV and 10 kHz, respectively.

B. Modes and typical regimes in MCP discharge

By summarizing the results obtained in the simulation as well as analyzing their spatial-temporal characteristics, the discharge modes along with their typical features and evolutions are obtained. Like previous reports, the discharge modes in MCP discharge are manifested to be either Townsend or glow. Besides, it is revealed that modes in MCP discharges are mainly dominated by gap width, while the role of voltage amplitude and driving frequency appear to be minor. Moreover, there are 2 typical and distinctive mode-combination regimes existing in these MCP discharges, which will be discussed in detail as follows.

When d_g is set to be relatively short (i.e. 1.6 mm or less, except for cases in which f is set within the order of 0.1 MHz), the first discharge regime, namely the 'MCP Townsend' regime shows up, whose typical waveforms can be seen in Figure 2, 3(b)–(f) and 4(c)-(f). In this regime, all the discharge peaks in each current pulse train operate at Townsend mode, in which the amplitude of current densities remain in the order of 0.1~1 mA·cm^{-2} or less, and the rising rate of each current pulse is relatively moderate. A further increase in d_g can lead to the mode of the incipient current peak switching into glow mode, thus converting the regime from 'MCP Townsend' into 'MCP glow', whose typical electrical characteristics are shown in Figure 4(a), (b). In this regime, the first discharge peak in each current pulse train is operated at glow mode, with a relatively large magnitude (a few or tens of mA·cm^{-2}), while the subsequent peaks might recover to Townsend discharge. For more insightful investigations, spatiotemporal distribution of electron density over one standard cycle of applied voltage is depicted in Figure 5 in order to obtain microscope properties, taking 1.6 mm and 2.2 mm gap as examples, where V_{am} and f are fixed at 2.0 kV and 10 kHz, respectively. As shown in Figure 5(a), in MCP Townsend regime, the distribution of electron density during each discharge pulse exhibits a cone shape, with high electron density area concentrating in the vicinity of instantaneous anode (i.e. x=0 during the positive half cycle of discharge current and x=d_g for the negative half), indicating a Townsend mode. Moreover, the maximum electron density during each pulse decreases relatively linearly from the 1st (1×10^{16} m^{-3}) to the 4rd pulse (about 1×10^{15} m^{-3}). While in MCP glow regime, as shown in Figure 5(b), the electrons during the 1st discharge peak exhibits a concentration near the instantaneous cathode, indicating a glow mode discharge. After the 1st peak, owing to the time

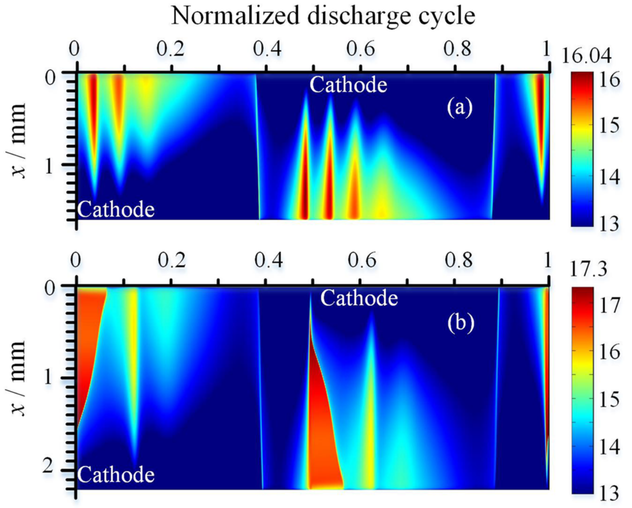

FIG. 5. Spatiotemporal distribution of logarithmic electron density ($\log_{10}(n_e)$) over one standard applied voltage cycle when d_g is set to be (a) 1.6 mm, (b) 2.2 m, where V_{am} and f are fixed at 2.0 kV and 10 kHz, respectively.

consumption of positive column dissipation,[7,47] the residual high-density area remains for a relatively long time, resulting in a longer time interval between 1st and 2nd current pulse compared with that at MCP-Townsend regime. Moreover, the reduction in maximum or average electron density between adjacent pulses is more remarkable compared with that in MCP Townsend regime, with maximum n_e being 2×10^{17} m^{-3} during the 1st pulse while reducing dramatically to about 5×10^{15} m^{-3} within the 2nd discharge pulse. Moreover, the electrons during the 2nd pulse are mainly concentrated beside the instantaneous anode, which demonstrates that the discharge is already converted to Townsend mode.

Figure 6 illustrates different contributions of the total discharge current at the instantaneous cathode and anode in both MCP Townsend (d_g=1.6 mm) and MCP glow regime (d_g=2.2 mm). As shown in Figure 6(a), (b), (c), in the vicinity of instantaneous cathode, the displacement current J_{disp} component contributes the most to the total current J_{tot} at the beginning of rising edge for the 1st current pulse. With the development of the breakdown process, the ion current commences to

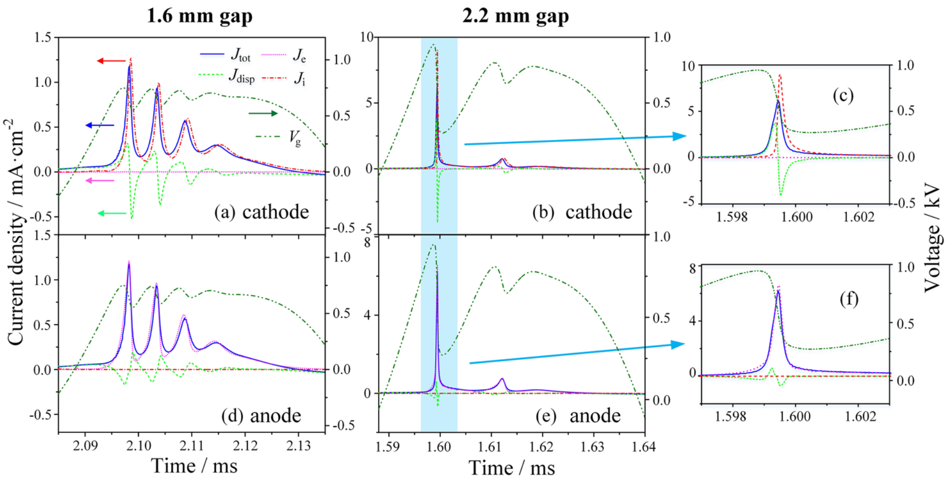

FIG. 6. Temporal profiles of positive current density components (J_{tot}: total current; J_{disp}: displacement current; J_e: electron current; J_i: ion current) at the boundaries of (a), (b), (c) instantaneous cathode and (d), (e), (f) anode in 1.6 mm and 2.2 mm gap. The V_{am} and f here are fixed at 2.0 kV and 10 kHz, respectively. (c) and (f) illustrate the partial zoom-in figures for the 1st current peak in (b) and (d), respectively.

dominate and ions flow onto the cathode boundary, neutralizing the cathode surface charges, thus leading to the impairment of cathode electric field as well as the sign of J_{disp} changing to negative.[8] Furthermore, as shown in Figure 6(a), the J_{i} curve basically accords with the J_{tot} curve after the 1st breakdown. In the MCP-glow regime, however, some distinctive differences can be found. As shown in Figure 6(b), (c), during the rising stage of the 1st current pulse, a strong J_{disp} is generated with the peak value surpassing 60% of J_{tot} amplitude, indicating a dramatic growth of electric field among the cathode layer. After the inversion of J_{disp}, J_{i} component continues to grow, being at most 1.45 times as large as the amplitude of J_{tot}, which should be attributed to the abundance of residual ions and sufficient field strength in the cathode layer. With a strong J_{i} prevailing, surface charges on the cathode dielectric surface are neutralized rapidly. After then, positive ions begin to accumulate on the cathode dielectric surface at a considerably high rate, shielding the electric field among the gap. As a result, the gap voltage V_{g} drops over 70% during the 1st pulse, as shown in Figure 6(c). While for Townsend discharge pulse, due to a lower deposition rate of surface charges, the resulting V_{g} drop is only about 25% of the maximum V_{g}, as shown in Figure 6(a). The severe decrease of V_{g} in the 2.2 mm case thereupon causes a relatively long recovering time of V_{g} as well as a long temporal interval between the 1st and 2nd breakdown, which might also contribute to the mode transition from glow to Townsend. On top of that, the current components at the instantaneous anode are illustrated in Figure 6(c), (d), (e), in which the current continuity is mainly sustained by the electron current in both glow and Townsend cases. The J_{disp} component plays a minor role here since the electric field is much weaker than that at the cathode.

C. Evolution trends and mechanisms with parameters varying in MCP discharges

1. *Influence of V_{am}*

To acquire more detailed information regarding the MCP evolution, the variation trajectories of some key parameters with external conditions varying are presented. Figure 7 illustrates the current density amplitude (J_{pm}), peak phase (Φ_{pm}) for the first current pulse and number of pulses per half cycle (N_{p}) with V_{am} altering. For clearer discussion, we divided the MCP evolution with V_{am} increasing into 4 distinctive stages and labelled in Figure 7. For stage I in which V_{am} value remains relatively low (0.8 kV-1.2 kV), the J_{pm} increases sharply while Φ_{pm} decreases rapidly with V_{am} increasing, during which the number of pulses per half cycle rises from 1 to 3. To qualitatively evaluate these phenomena, the breakdown criteria is required. Note that before the ignition of the 1st discharge, the J_{disp} component dominates, as shown in Figure 6. Therefore, the breakdown criteria can be determined by the series capacitors approximation,[17,20,48] given by:

$$V_{\mathrm{gb}} = \frac{d_{\mathrm{g}}}{d_{\mathrm{g}} + 2d_{\mathrm{b}}/\varepsilon_{\mathrm{r}}} V_{\mathrm{am}} \sin(\phi_{\mathrm{b}}) = D(d_{\mathrm{g}}) \cdot V_{\mathrm{am}} \sin(\phi_{\mathrm{b}}) \tag{15}$$

where V_{gb} represents the breakdown voltage (over the gap), Φ_{b} stands for the corresponding phase at the moment of breakdown. ε_{r} is the relative permittivity of dielectric layer. D is a ratio representing

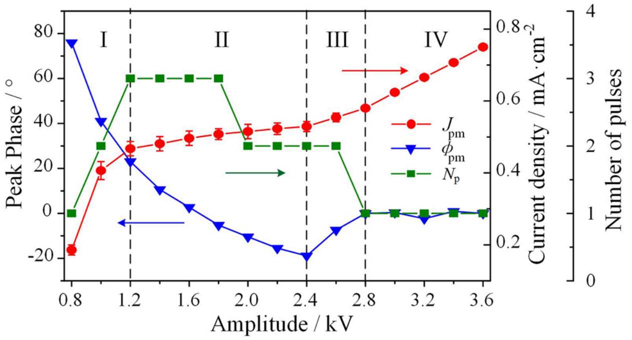

FIG. 7. Evolution trends of current density amplitude (J_{pm}), peak phase (Φ_{pm}) for the first current peak and number of pulses per half cycle (N_{p}) with V_{am} altering, where f and d_{g} are fixed at 10 kHz and 1 mm, respectively.

the proportion of total applied voltage that drops across the gas gap when treating dielectrics and gas gap as capacitors in series. The solution of Φ_{b} is expressed as follow:

$$\phi_{\mathrm{b}} = \sin^{-1}\left(\frac{V_{\mathrm{gb}}}{D(d_{\mathrm{g}}) \cdot V_{\mathrm{am}}}\right) \tag{16}$$

Moreover, the relationship between Φ_{pm} and Φ_{b} can be approximately expressed by:

$$\phi_{\mathrm{pm}} = \phi_{\mathrm{b}} + \phi_{\mathrm{r}} \tag{17}$$

in which Φ_{r} represents the rising phase between the breakdown and peak moment of the 1st discharge. Note that V_{gb} is mainly determined by the gap width, and an increase in V_{am} actually leads to slightly decrease in V_{gb} due to the enhanced seed electron and metastable concentrations before the ignition of pulses.[8,12] In that case, with the increase of V_{am}, Φ_{b} decreases. Furthermore, the rising phase Φ_{r} depends mainly on V_{am} and d_{g}, and an increasing in V_{am} leads to shorter rising time and hence smaller Φ_{r}.[16,49] Therefore, when increasing V_{am} in stage I, both Φ_{b} and Φ_{r} decreases, leading to the decline of Φ_{pm}. Besides, the number of pulses per half cycle N_{p} should, according to previous reports,[9,12] be closely associated with the time duration between the ignition of 1st pulse and the peak of applied voltage T_{mcp}, written by:

$$T_{\mathrm{mcp}} = \frac{90^{\circ} - \phi_{\mathrm{pm}}}{360^{\circ}} \times \frac{1}{f} \tag{18}$$

With Φ_{pm} decreasing, T_{mcp} rises, indicating the time available for the development of subsequent breakdowns is prolonged, providing a more suitable situation for MCP discharges. Moreover, the enhanced concentrations of free electrons, metastable particles as well as surface charges with the increase of external voltage also contribute to the generation of pulses. Those factors interact together and give rise to the increase of N_{p} in this stage.

With V_{am} exceeding 1.2 kV the discharge evolves into stage II. In this stage, the increase of pulse number ceases, while the time intervals between peaks start to decrease, and pulses tend to overlap each other. Moreover, the increase of J_{pm} with V_{am} rising tends to saturate. One possible explanation on the merging of current pulses is associated with the sinusoidal component of the total current (i_{tot}), which can be evaluated by expressing i_{tot} via the capacitance current through the dielectrics (i_{d}):[18,20]

$$V_{\mathrm{d}} = V_{\mathrm{a}} - V_{\mathrm{g}} \tag{19}$$

$$i_{\mathrm{tot}} = i_{\mathrm{d}} = C_{\mathrm{d}}\frac{\mathrm{d}V_{\mathrm{d}}}{\mathrm{d}t} = \frac{\varepsilon_{0}\varepsilon_{\mathrm{r}} \cdot S}{2d_{\mathrm{b}}} \cdot \frac{\mathrm{d}V_{\mathrm{d}}}{\mathrm{d}t} \tag{20}$$

where V_{d} represents the total voltage drop on the dielectrics, C_{d} is the total equivalent capacitance of dielectrics. S is the area of electrode. Simultaneously consider equation (19) and (20) yields:

$$i_{\mathrm{tot}} = \frac{2\pi f \cdot \varepsilon_{0}\varepsilon_{\mathrm{r}} \cdot S}{2d_{\mathrm{b}}} \cdot V_{\mathrm{am}}\cos(2\pi f t) - \frac{\varepsilon_{0}\varepsilon_{\mathrm{r}} \cdot S}{2d_{\mathrm{b}}} \cdot \frac{\mathrm{d}V_{\mathrm{g}}}{\mathrm{d}t} \tag{21}$$

The first term on the right side of equal sign represents the contribution of capacitive sinusoidal component J_{sin}, while the second term is related to the changing rate of V_{g}, behaving a pulsed feature (denoted as J_{pul}). As V_{am} increases, the sinusoidal component enhances linearly with V_{am}, which helps to elevate the current density at current troughs and smooth the current waveform (i.e. reduce N_{p}). As regards the second term, due to the limitation of V_{gb} ($V_{\mathrm{g}} \leq V_{\mathrm{gb}}$), its effect on V_{d} as well as on the total current weakens with V_{am} increasing. For clearly expression, Figure 8 illustrates the comparison between simulation data of J_{pm} and the amplitude of J_{sin} calculated by the expression shown in equation (21). Apparently, the discrepancy between J_{pm} and J_{sin} is reduced significantly in the stage II. With the sinusoidal component enhancing its weight in total current, pulses previously separated incline to overlap and give rise to the increase of the total pulse width as well as the decrease of separated pulse number. Besides, the reduced proportion of pulsed current component due to the limitation of V_{g} also lead to the saturation of current density amplitude of J_{pm}, as shown in Figure 7.

As V_{am} goes in exceed of 2.4 kV, the discharge turns into stage III, in which the value of Φ_{pm} starts to rebound and the discharge recovers to single peak at 2.8 kV, as shown in Figure 7.

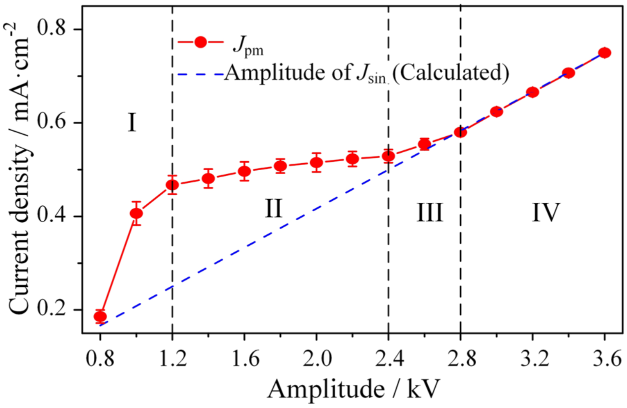

FIG. 8. Comparison between the total current density amplitude (J_{pm}) and calculated amplitude of sinusoidal current component (J_{sin}) for the first current peak with voltage amplitude V_{am} altering, where f and d_g are fixed at 10 kHz and 1 mm, respectively.

The overlap of current pulses becomes remarkable, with only a minor oscillation of current density in the vicinity of first current pulse. Owing to the growing merging effect, Φ_{pm} experiences a rebound in this stage mainly because of the overlap between the 1st and its subsequent pulses, thus enhancing the corresponding rising time as well as delaying the peak phase.

Further increase the V_{am} makes the discharge transforming into the stage IV, in which the waveform of discharge current tends to stabilize with a wide single pulse per half cycle and a quasi-sinusoidal shape, and Φ_{pm} is kept fixing at 0 degree. Those phenomena are mainly attributed to the predominance of sinusoidal current component in total current. As illustrated in Figure 8, in stage IV, the J_{sin} curve converges completely with the simulation data of J_{pm}, indicating a dominant contribution of sinusoidal current component over the total current, while the proportion of pulsed current component in J_{tot} is almost eliminated. For further investigation, Figure 9 depicts the temporal profiles of surface charges (in Figure 9(a)) along with the waveforms of V_a, V_g, V_d and J_{tot} (in Figure 9(b)). As it can be seen, a sinusoidal-shaped current pulse leads to a moderate charge neutralization rate (quasi-sinusoidal) on the dielectric surfaces during the discharge phase, so does the increasing rate of the voltage drop on dielectrics (since $|V_d| \sim (|\sigma_{su}|+|\sigma_{sl}|)/2C_d$, and the sign of V_d is negative at the beginning of this phase). Therefore, the effect of surface charge neutralization on the drop of V_g can be offset by the sinusoidal increase of external voltage (since $V_g=V_a-V_d$). As a result, the V_g waveform is smoothed and the changing rate dV_g/dt remains almost 0 from the breakdown moment to the peak moment of applied voltage in stage IV, as shown in Figure 9(b), indicating that the contribution of pulsed current component to J_{tot} is eliminated. With the absolute dominance of sinusoidal current component, the total current behaves a thoroughly capacitive sinusoidal characteristic, forcing the peak phase Φ_{pm} shifting to 0°.

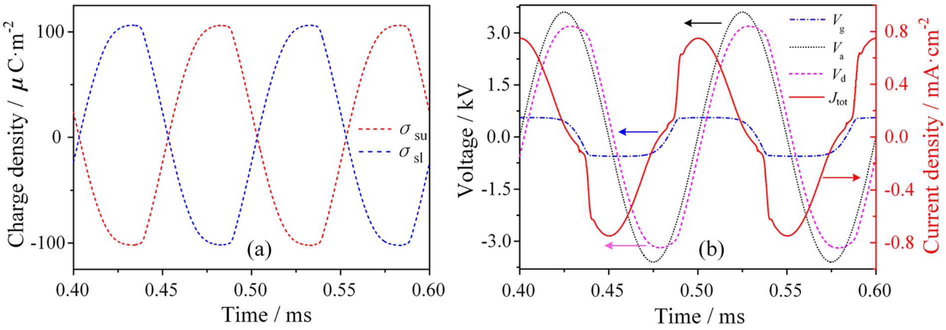

FIG. 9. Temporal profiles of (a) surface charge densities on upper dielectric surface (σ_{su}) and lower surface (σ_{sl}) as well as (b) waveforms of V_g, V_a, V_d and J_{tot} over 2 standard applied voltage cycle.

2. Influence of f

The evolution trajectories of J_{pm}, Φ_{pm} as well as N_{p} with f altering are plotted in Figure 10. Based on the variation characteristics of parameters, 3 distinctive stages are determined here. For the stage at which the driving frequency is relatively low (under 5 kHz), N_{P} experiences a dramatic decrease, especially under 1 kHz, with f increasing, and the J_{pm} curve increases with a relatively large slope, while Φ_{pm} encounters a slightly elevation as f enhances. The evolution of N_{p} in this stage can still be explained using equation (15)–(21): when f is set to be extremely low, the time duration for MCP generation T_{mcp}, known from equation (18), is sufficiently long, and the sinusoidal component J_{sin} in the total current, which helps to smooth the current pulse and restrains the emerge of current pulses, is negligible (known from equation (21)). Therefore, the multi-peak thrives in this stage. However, within a low-frequency band, a slight increase in f can cause a conspicuous drop of T_{mcp}, thereby inducing a dramatic decrease in N_{p}, which is especially the case when f is under 1 kHz. Besides, the slight delay of peak phase in this stage should be attributed to the increase of rising time for the 1st current pulse due to the overlap of pulses, yielding a larger Φ_{r} and, in consequence, a larger Φ_{pm}.

If f is increased to above 15 kHz, the stage II replaces the former one. The evolution trajectories in stage II is very similar with that of stage II illustrated in Figure 7. Such similarity is mainly originated from the identical evolution trend on the contribution of sinusoidal current component to the total current. To be specific, as f increases in this stage, the sinusoidal component increases linearly, which, along with the decline of T_{mcp}, promotes the smoothing of current waveform as well as the decrease of N_{p}. The saturation of J_{pm} in this stage is induced by the reduced contribution of pulsed current component due to the smoothed V_{g}, as stated in Section III.C.1.

A further increase in f brings about the advent of stage III. In this stage, the sinusoidal current component gradually grab the dominance due to the advanced f. As a result, the N_{p} number downs to very low while J_{pm} rises linearly with f increasing. Also, Φ_{pm} gradually converges to 0 degree, behaving a purely capacitive feature. Another noteworthy phenomenon is that a relatively sharp current pulse instead of a sinusoidal one is observed when f rises to the order of 0.1 MHz, as shown in Figure 3(a), which is against the prediction made by equation (21). This contradiction is primarily resulted from the intensified influence of space charge effect. Figure 11 depicts the spatiotemporal distribution of electron density for driving frequency set at 300 kHz and 40 kHz. Due to the time reduction in each discharge half cycle, a substantial amount of free electrons are trapped in the gap before the next breakdown. These trapped electrons flow back to the previous cathode (i.e. x=1.0 mm), inducing an obvious 'residual current peak' before the main pulse occurs, as shown in Figure 3(a), and provide a large amount of seed electrons to the subsequent discharge. Hence, the average electron density at the beginning moment of each breakdown in 300 kHz case is about 2 orders as large as that of 40 kHz case, as shown in Figure 11(a) and (b), respectively. With a high seed electron level in the gap as well as low reactance within the discharge circuit, a glow discharge instead of a Townsend one is generated in the main peak, with the maximum electron density area locating near the instantaneous

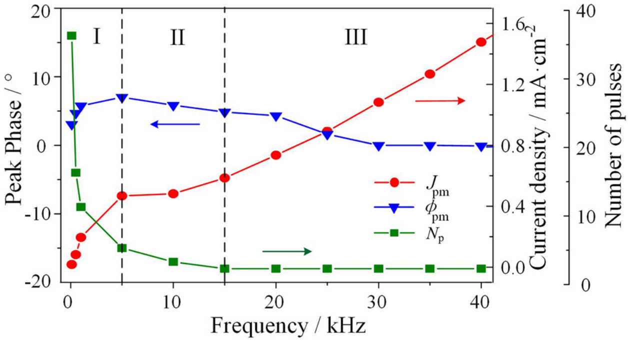

FIG. 10. Evolution trends of current density amplitude (J_{pm}) and peak phase (Φ_{pm}) for the first current peak and number of pulses per half cycle (N_{p}) with f altering, where V_{am} and d_{g} are fixed at 1.5 kV and 1 mm, respectively.

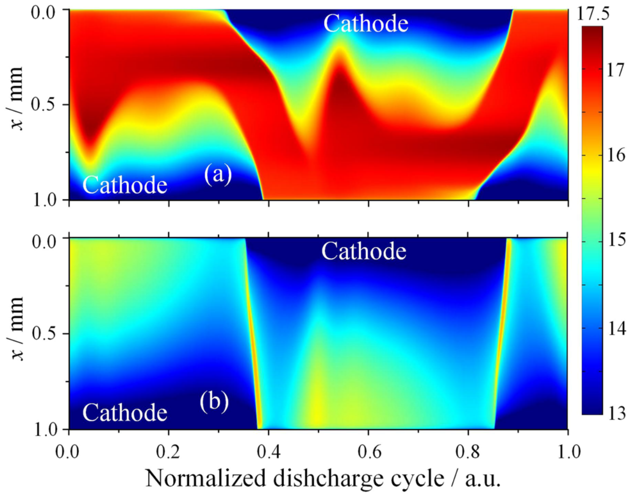

FIG. 11. Spatiotemporal distribution of logarithmic electron density ($\log_{10}(n_e)$) over one standard applied voltage cycle when f is set to be (a) 300 kHz, (b) 40 kHz, where V_{am} and d_g are fixed at 2.0 kV and 1 mm, respectively.

cathode, as shown in Figure 11(a), which is markedly different from that at Townsend mode, as illustrated in Figure 11(b). Therefore, the space charge effect is greatly strengthened within a short phase, yielding a sharp discharge pulse. This phenomenon agrees well with the result of previous study performed by Jiang *et al.*[13]

3. Influence of d_g

Figure 12 plots the evolution trajectories of J_{pm}, Φ_{pm} as well as N_p with d_g altering, corresponding to the parametric simulation with regard to Figure 4. There are 4 distinctive stages divided in Figure 12. In the incipient stage where gap width is kept relatively low, both Φ_{pm} and N_p decrease sharply with d_g increasing from a large number to moderate or minimum, while a slight drop in J_{pm} is perceived simultaneously. In super narrow gaps ($d \leq 0.2$ mm), with a rapid transportation rate of species as well as quasi-homogeneous distribution of electric field, the electrical and dynamic characteristics of the discharge are quite different from that of discharges with larger gaps. For more insightful discussion, Figure 13 illustrates the waveforms of different current components at instantaneous cathode and anode as well as V_g within the positive current pulse train. As it can be seen, in 0.1 mm case, J_{tot}, J_{disp} as well as conductive current component(J_e or J_i), with steep pulses, reach their peaks synchronously, indicating a fast response of pulsed current component. Moreover, in the first few discharge troughs, as shown in Figure 13(a), (c), due to the abrupt drop in V_g, the conductive current

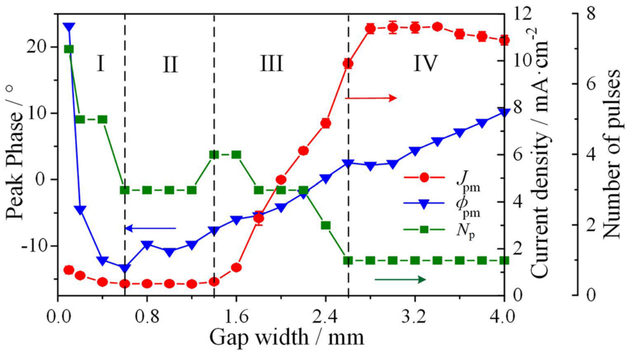

FIG. 12. Evolution trends of current density amplitude (J_{pm}) and peak phase (Φ_{pm}) for the first current pulse and number of pulses per half cycle (N_p) with d_g altering, where V_{am} and f are fixed at 2.0 kV and 10 kHz, respectively.

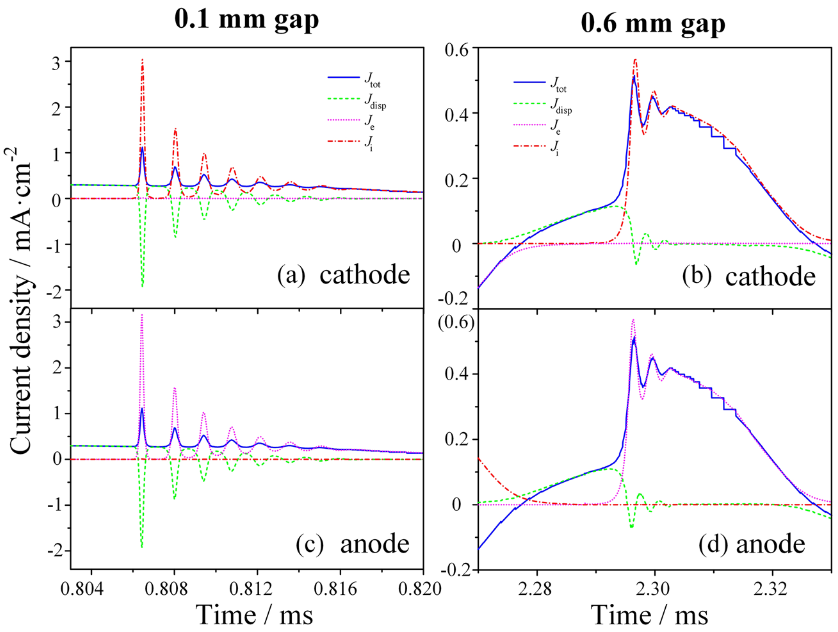

FIG. 13. Temporal profiles of current density components (J_{tot}: total current; J_{disp}: displacement current; J_{e}: electron current; J_{i}: ion current) during the positive half at the boundaries of (a), (b) instantaneous cathode and (c), (d) anode in 0.1 mm and 0.6 mm gap. The V_{am} and f here are fixed at 2.0 kV and 10 kHz, respectively.

components drop to almost 0 while J_{disp} contributes most of total current, whereas in 0.6 mm case the conductive current components are still considerably high at troughs. These features indicate that the discharge in the vicinity of first few troughs in 0.1 mm case are extinguished. The abrupt quench among current peaks helps to separate individual pulses and, along with the extremely short pulse width, promotes the abundance of current pulses per half cycle under this circumstance. A slight increase in d_{g} in this stage, however, can cause a considerable increase in the rising time of pulses as well as pulse width, which tends to mitigate the abrupt quench at current troughs and smooth the current waveform. This might result in the vast decline in N_{p} in this stage.

The evolution trend of Φ_{pm} in this stage can be explained using equation (16) and (17). As it can be seen, for fixed V_{am} and f, Φ_{b} is determined by the competition between V_{gb} and $D(d_{\mathrm{g}})$. The simulation data of V_{gb} as a function of d_{g} as well as the corresponding linear fit are illustrated in Figure 14. Apparently, a quasi-linear variation of V_{gb} is perceived, which is similar to the right half of a standard Paschen curve. Taking the linear fitting curve of V_{g}-d_{g} and other relevant constant

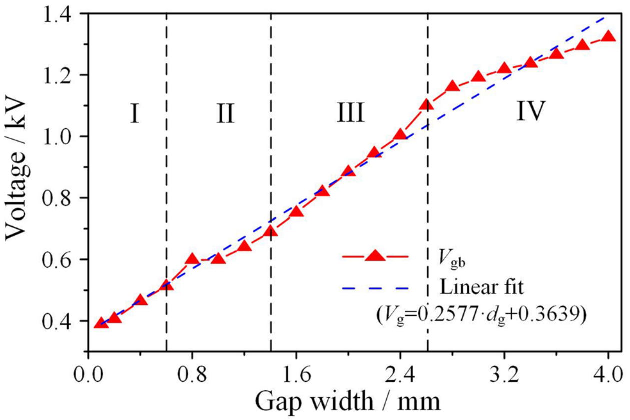

FIG. 14. Evolution trends of breakdown voltage (V_{gb}) for the 1st current peak with d_{g} altering and its linear fit.

parameters into equation (16) yields:

$$\phi_b{}^* = \sin^{-1}\left(\frac{0.2577d_g + 0.3639}{\dfrac{1}{1 + 2/7.5d_g} \times 2}\right) \tag{22}$$

The calculated $\Phi_b{}^*$ curve using equation (22) and simulation data of Φ_{pm} are depicted in Figure 15. An approximate average deviation 33.8° is subtracted from $\Phi_b{}^*$ in favour of direct comparison. As is illustrated in Figure 15, the $\Phi_b{}^*$-33.8° curve exhibits a great consistency with the simulation data of Φ_{pm}, manifesting the accuracy and applicability of equation (16) and (17) in this circumstance. The global deviation 33.8° is mainly attributed by the surface polarization induced by the conductive current, which elevates the electric field among the gap before the ignition of the 1st discharge, and promotes the current peaks coming in advance. Moreover, the rising phase Φ_r appears to be so minor compared with the breakdown phase Φ_b so that we can assume $\Phi_{pm} \approx \Phi_b$. Therefore, the $\Phi_b{}^*$-33.8° curve in Figure 15 seems to be directly consistent with simulation data of Φ_{pm}.

When d_g is increased to be over 0.6 mm the discharge evolves into stage II, during which the J_{pm} keeps basically unvaried while the discrepancy between current peaks and troughs enlarges and N_p tends to increase, whereas the peak phase delays with d_g increasing. The abrupt increase in N_p value in this process is somehow contradictory with the common knowledge that an increase in d_g should lead to the decrease of N_p. Note that the differences between current peaks and troughs tend to enlarge and voltage drop in V_g after each breakdown becomes more severe in this stage, as shown in Figure 4(d), (e), (f), which also provide a possible clue to uncover the mechanism regarding N_p's abnormal variation. To be specific, the increase of d_g in this stage might result in some subtle changes in discharge dynamics, which helps to suppress the current density at troughs and causes the enlargement of difference between current peaks and troughs. As a result, the separation of pulses is promoted and N_p starts to rebound in this stage. More in-depth explanation on this issue is still missing and requires further investigation.

The stage III arises when d_g is set within 1.4 ~ 2.6 mm. In this stage, N_p decreases monotonously with d_g increasing and the discharge recovers to single-peak when d_g reaches 2.6 mm, while a dramatic increase in J_{pm} is perceived. As stated in Section III.B, a discharge regime transition between MCP-Townsend and MCP-glow takes place when d_g reaches 1.8 mm, switching the 1st discharge peak into glow mode. Therefore, the 1st current peak is greatly strengthened, leading to a jump up of J_{pm} at d_g=1.8 mm. With the further increase of d_g in this stage, the glow discharge structure is further strengthened, which enhances the influence of space charge effect on discharge dynamics and forms a continuously increasing J_{pm} curve. Besides, the decrease of N_p in this stage is mainly attributed to the delaying Φ_{pm} (i.e. decreasing T_{mcp}). Also, with prolonged inter-pulse time between the

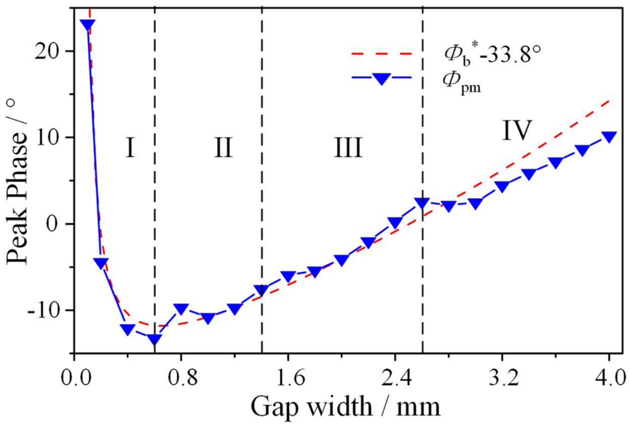

FIG. 15. Comparison between the current peak phase (Φ_{pm}) and calculated breakdown phase ($\Phi_b{}^*$) curve using equation (22) for the first current pulse with d_g altering. An average deviation 33.8° is subtracted from $\Phi_b{}^*$ in favour of direct comparison.

1^{st} and 2^{nd} current peak in MCP-glow regime, as shown in Figure 6, the time span available for the generation of subsequent discharges is further cut down, which also contribute to the decrease of N_p with d_g increasing in this stage.

With d_g enlarges in exceed of 2.6 mm the discharge evolves into the last stage, in which the discharge have already recovered to single-peak mode. The J_{pm} tends to saturate and then decreases, and Φ_{pm} increases monotonously with d_g increasing. Note that in sufficient large gaps, the glow discharge structure is fully developed. In that case, an increase in d_g promotes neither the space charge effect within the cathode sheath, nor the current amplitude, which now appears to be more sensitive to the decrease of average electric field among the gap ($E_{avg}=DV_a \cdot d_g^{-1}$). This explains the evolution of J_{pm} in this stage.

4. Factors that affects N_p, Φ_{pm}, and J_{pm}

Summarizing the results obtained in above-mentioned parametric analyses, the typical influence factors for N_p, Φ_{pm}, and J_{pm} are integrated and listed as follows:

1) N_p. The number of pulses per discharge half cycle N_p is found to be affected by the peak phase of first discharge Φ_{pm}, pulse width as well as the proportion of sinusoidal current component J_{sin} expressed in equation (21). The decrease in Φ_{pm} leads to the increase of total time available for the generation of MCP (T_{mcp}), as given in equation (18), thus elevating N_p. Moreover, an increase in V_{am} or f is found in favour of enhancing the contribution of J_{sin} to the total current, giving rise to the smoothing of current waveform as well as the overlap of individual pulses, thus causing the decrease of N_p.
2) Φ_{pm}. The peak phase for the first current pulse in a certain current pulse train Φ_{pm} is determined by its corresponding breakdown phase Φ_b and the rising phase Φ_r, known from equation (17). To be specific, Φ_b is mainly dominated by the competition between V_{gb} and $D(d_g) \cdot V_{am}$, as shown in equation (16), and the effect of surface polarization caused by the conductive current helps to bring forward the 1^{st} breakdown and reduce $\Phi_{b.}$ For rising phase Φ_r, typically, a decrease in d_g or an increase in V_{am} lead to the reduction of Φ_r, and a mode transition from Townsend to glow also helps to cut down Φ_r. In most cases, Φ_r plays a minor role in determining the peak phase due to its limited proportion in total Φ_{pm}.
3) J_{pm}. According to equation (21), the total discharge current density is composed of sinusoidal current component J_{sin} and pulsed current component J_{pul}. From this perspective, the variation of J_{pm} is affected by the superposition of J_{sin} and J_{pul}. For J_{sin} whose peak phase is fixed at 0°, the amplitude is positively associated with f and V_{am}. While for J_{pul}, its amplitude and peak phase relies on the changing rate of V_g.

IV. CONCLUSIVE REMARKS

In this paper, a one-dimensional self-consistent fluid model is applied to systematically investigate the characteristics and dynamics of multiple-current-pulse (MCP) phenomenon generated by homogeneous dielectric barrier discharge (HDBD) as well as its evolution mechanisms. Some important conclusions are draw as follows:

1) Two typical discharge regimes, namely the MCP-Townsend and MCP-glow, with different arrangement of discharge modes (Townsend or glow) among current pulses, are discovered in MCP discharges. In MCP-Townsend regime, all the discharge peaks operate at Townsend mode, with a relatively gentle rising rate of current pulses and moderate gap voltage (V_g) drop during the pulsing time, and conductive current component (electron current J_e or ion current J_i) curves basically coincide with the total current (J_{tot}) curve. In MCP-glow regime, the first discharge peak operates at glow mode, while for subsequent pulses the discharge at peak moments could recover to Townsend mode through a glow-Townsend transition. Moreover, the glow-driven current pulse exhibits a relatively large amplitude and a steep rising edge, and the mismatch in peak phase and amplitude between J_i and J_{tot} in the vicinity of instantaneous cathode is more remarkable compared with that of Townsend-driven pulses. Owing to the strong conductive current, the voltage drop in V_g during the glow discharge pulse is much more severe

compared with that of Townsend-driven pulses, which suppresses the development of subsequent breakdowns and delays the incoming of next breakdown, also contributes to glow-Townsend mode transition.

2) By altering the voltage amplitude with other external conditions remain unvaried, the influence of voltage amplitude (V_{am}) on the MCP behavior is studied. It is revealed that with the increase of V_{am}, the discharge evolves from a single-pulse one into MCP discharge, and then returns to single-peak discharge with a quasi-sinusoidal current waveform at higher voltages through a pulse merging process. The merging effect among pulses is mainly attributed to the elevated proportion of sinusoidal current component J_{sin} in the total current, which helps to elevate the current density at current troughs and smooth the current waveform, thus reducing the number of pulses per half cycle (N_{p}).
3) An increase in driving frequency f is found restraining the generation of MCP in the whole frequency range. When f is within a low-frequency band (<1 kHz), the MCP thrives with N_{P} exceeding 30 at maximum, while rising f in this stage brings about a dramatic decrease in N_{p}. Further increase f leads to a continuous decrease in N_{p}, with reduced decline rate. Those phenomena are initiated mainly by the shortening time duration for MCP generation as well as the enhancing weight of sinusoidal current component J_{sin} in the total current as f increases. Besides, a relatively sharp current pulse instead of a sinusoidal one is observed when f is risen to the order of 0.1 MHz, which is against the previous prediction. A mode conversion from Townsend to glow due to the enhanced seed electron level as well as relatively low reactance within the discharge circuit is considered responsible for this phenomenon.
4) A non-monotonic evolution of N_{p} is perceived when d_{g} is set as the controlling parameter. In particular, when increasing d_{g} from 0 to 4 mm, the N_{p} value decreases vastly in the first place, while experiencing a slight enhancement within a short d_{g} window, and continues to go down afterwards. The subtle mechanism for such evolution is rather complicated and might attributed to the evolution of pulse width and its resulting voltage drop among the gap. The variation of Φ_{pm} is found to be dominated by the competition between the breakdown voltage V_{gb} and the product of D and V_{am} (D represents the proportion of total applied voltage that drops across the gas gap). Moreover, an abrupt and dramatic increase in J_{pm} is observed when d_{g} enhances within 1.6~2.6 mm, which is caused by the mode conversion from Townsend to glow and gradually strengthened space charge effect.

ACKNOWLEDGMENTS

This work is supported by the State Key Laboratory of Alternate Electrical Power System with Renewable Energy Sources (Grant No. LAPS17005) and the Fundamental Research Funds for the Central Universities (Grant No. 2017BQ42).

[1] Y. Liu, Z. Fang, and L. Cai, High Voltage Engineering **38**, 1141 (2012).
[2] T. Shao, C. Zhang, K. Long, D. Zhang, J. Wang, P. Yan, and Y. Zhou, Applied Surface Science **256**, 3888 (2010).
[3] N. Y. Babaeva, W. Tian, and M. J. Kushner, Journal of Physics D: Applied Physics **47**, 235201 (2014).
[4] A. V. Nastuta, I. Topala, C. Grigoras, V. Pohoata, and G. Popa, Journal of Physics D: Applied Physics **44**, 105204 (2011).
[5] X. P. Lu, High Voltage Engineering **37**, 1416 (2011).
[6] B. Jiang, J. Zheng, S. Qiu, M. Wu, Q. Zhang, Z. Yan, and Q. Xue, Chemical Engineering Journal **236**, 348 (2014).
[7] Y. B. Golubovskii, V. A. Maiorov, J. Behnke, and J. F. Behnke, Journal of Physics D: Applied Physics **36**, 39 (2003).
[8] L. Mangolini, C. Anderson, J. Heberlein, and U. Kortshagen, Journal of Physics D: Applied Physics **37**, 1021 (2004).
[9] J. Shin and L. L. Raja, Journal of Applied Physics **94**, 7408 (2003).
[10] Y. Zhang, B. Gu, X. Peng, D. Wang, and W. Wang, Thin Solid Films **516**, 7547 (2008).
[11] Y. S. Akishev, Plasma Physics Reports **27**, 170 (2001).
[12] I. Radu, R. Bartnikas, and M. R. Wertheimer, IEEE Trans. on Plasma Science (2003).
[13] W. M. Jiang, J. Tang, Y. S. Wang, W. Zhao, and Y. X. Duan, Physics of Plasmas **20**, 073509 (2013).
[14] Y. Zhang, B. Gu, W. Wang, D. Wang, and X. Peng, Journal of Applied Physics **106**, 023307 (2009).
[15] D. Wang, Y. Wang, and C. Liu, Thin Solid Films **506-507**, 384 (2006).
[16] D. Dai, Y. Zhang, and W. Ning, High Voltage Engineering **43**, 1766 (2017).
[17] R. Bartnikas and J. P. Novak, IEEE Trans. on Dielectrics and Electrical Insulation **27**, 3 (1992).
[18] R. Bartnikas, Archiv für Elektrotech. **52**, 348 (1969).
[19] R. Bartnikas and G. L. d'Ombrain, IEEE Transactions on Power Apparatus and Systems **84**, 770 (1965).
[20] Y. T. Zhang, D. Z. Wang, and M. G. Kong, Journal of Applied Physics **100**, 063304 (2006).

[21] D. Petrović, T. Martens, J. van Dijk, W. J. M. Brok, and A. Bogaerts, Journal of Physics D: Applied Physics **42**, 205206 (2009).
[22] D. Zhang, Y. Wang, and D. Wang, Chinese Physics B **26**, 065206 (2017).
[23] S. Gadkari and S. Gu, Physics of Plasmas **24**, 053517 (2017).
[24] W. Yan, Y. Xia, Z. Bi, Y. Song, D. Wang, E. A. Sosnin, V. S. Skakun, and D. Liu, Journal of Physics D: Applied Physics **50**, 345201 (2017).
[25] Z. Huang, Y. Hao, L. Yang, Y. Han, and L. Li, Physics of Plasmas **22**, 1235009 (2015).
[26] C. Lazarou, T. Belmonte, A. S. Chiper, and G. E. Georghiou, Plasma Sources Science and Technology **25**, 055023 (2016).
[27] C. Lazarou, D. Koukounis, A. S. Chiper, C. Costin, I. Topala, and G. E. Georghiou, Plasma Sources Science and Technology **24**, 035012 (2015).
[28] M. A. Lieberman and A. J. Lichtenberg, *Principles of Plasma Discharges and Materials Processing*, Vol. 2nd (Wiley, Hoboken, NJ, 2005).
[29] G. J. M. Hagelaar and L. C. Pitchford, Plasma Sources Science and Technology **14**, 722 (2005).
[30] Y. P. Raizer, *Gas discharge physics* Vol. 1 (Springer, Berlin, 1991).
[31] H. W. Ellis, R. Y. Pai, E. W. McDaniel, E. A. Mason, and L. A. Viehland, Atomic Data and Nuclear Data Tables **17**, 177 (1976).
[32] https://www.lxcat.net/IST-Lisbon database. (Accessed on July 21, 2017).
[33] G. J. M. Hagelaar, Physical Review E **62**, 1452 (2000).
[34] H. Motz and H. Wise, The Journal of Chemical Physics **32**, 1893 (1960).
[35] R. Deloche, P. Monchicourt, M. Cheret, and F. Lambert, Physical Review A **13**, 1140 (1976).
[36] X. Yuan and L. L. Raja, IEEE Trans. on Plasma Science **31**, 495 (2003).
[37] Q. Wang, D. J. Economou, and V. M. Donnelly, Journal of Applied Physics **100**, 023301 (2006).
[38] T. J. Millar, P. R. A. Farquhar, and K. Willacy, Astronomy and Astrophysics Supplement Series **121**, 139 (1997).
[39] F. J. Gordillo-Vázquez, Journal of Physics D: Applied Physics **41**, 234016 (2008).
[40] R. S. Konstantinovskii, V. M. Shibkov, and L. V. Shibkova, Kinetics and Catalysis **46**, 775 (2005).
[41] K. R. Stalder, R. J. Vidmar, G. Nersisyan, and W. G. Graham, Journal of Applied Physics **99**, 093301 (2006).
[42] T. Martens, A. Bogaerts, W. J. M. Brok, and J. V. Dijk, Applied Physics Letters **92**, 041504 (2008).
[43] T. Martens, A. Bogaerts, W. J. M. Brok, and J. van Dijk, Applied Physics Letters **96**, 091501 (2010).
[44] http://www.comsol.com/plasma-module/.
[45] C. G. Petra, O. Schenk, M. Lubin, and K. Gäertner, SIAM Journal on Scientific Computing **36**, C139 (2014).
[46] C. G. Petra, O. Schenk, and M. Anitescu, IEEE Computing in Science & Engineering **16**, 32 (2014).
[47] D. Dai, H. X. Hou, and Y. P. Hao, Applied Physics Letters **98**, 131503 (2011).
[48] H. Luo, Z. Liang, X. Wang, Z. Guan, and L. Wang, Journal of Physics D: Applied Physics **43**, 155201 (2010).
[49] R. Bartnikas and J. P. Novak, IEEE Trans. on Dielectrics and Electrical Insulation **2**, 557 (1995).